Temperature-dependent resistive switching behavior of a hybrid semiconductor-oxide planar system

S. Majumder[1] · K. Kumari[1] · S. J. Ray[1]

Abstract

In this work, we have reported the temperature-dependent resistive switching (RS) behavior observed in $(1-x)CuI.(x)La_{0.7}Sr_{0.3}MnO_3$ nanocomposites with $0.001 < x < 0.05$ within the temperature range of 150 K to 300 K. Here, we observed bipolar and interface-type RS behavior, where the resistance can be altered to its previous state by the application of an opposite bias voltage. The extensive analysis of the current versus voltage data for different compositions at room temperature revealed that the dominating transport mechanisms in the low and high bias regions, respectively, were Schottky emission and Poole–Frenkel effect. The enhanced switching response of the RS medium after the addition of $La_{0.7}Sr_{0.3}MnO_3$ can be attributed to the oxygen vacancy-induced conduction which was confirmed by X Ray Photoelectron Spectroscopy (XPS) measurements. In the endurance test, the highest ON/OFF ratio averaged over 100 cycles was observed to be 4.2 ± 1.1 and 3.8 ± 0.3 for $x = 0.001$ and 0.02 respectively at $T = 300K$. At $T = 250$ K, we obtained the optimal ON/OFF ratio of 19.8 ± 1.8 for $x = 0.001$ and 22.7 ± 4.1 for $x = 0.02$. The investigation of current versus voltage graphs for $T = 250$ K, 200 K, and 150 K further confirmed Schottky emission and the Poole–Frenkel effect as the dominating transport mechanisms at lower temperatures.

1 Introduction

In the past few decades, memory devices' performance and processing power have advanced tremendously in terms of superior speed, lower power consumption, and down-scaling of the chip size. However, conventional semiconductor-based memories such as DRAM (dynamic random access memory), SRAM (static random access memory), and NAND flash memory have already reached the threshold of the down-scaling limit predicted by Moore's law and also face additional shortcomings like heat death, and excessive costs for the manufacturing of ultra-large-scale projects, insusceptibility to strain on the devices. This led scientists to a venture for building alternative memory devices/architectures that can satisfy the ever-increasing need for more powerful processing power in digital/analog electronics, neural networks, data storage, artificial intelligence,

etc. [1–4]. Therefore, it has become necessary to fabricate a 'universal memory' that can operate at high speed with density circuitry and possess non-volatile storage capacity, thus incorporating the merits of different popular memory devices into a single one. Therefore, the emergence of new NVM (non-volatile memory devices) such as phase-change random access memory (PCRAM) [5, 6], spin-transfer torque magnetic RAM (STT-MRAM) [7, 8], ferroelectric RAM (FRAM) [9], resistive RAM (RRAM or ReRAM) [10–12] and conducting bridge RAM (CBRAM) [13] is gaining huge momentum worldwide. Among the members of the NVM memory family, resistive switching-based memory has attracted huge attention owing to its comparatively easy fabrication process and proven compatibility with CMOS technology [14], competence for high-density packing of chips through cross-point structure [15], superior performance-like higher switching speed (< 10 ns) [16], scalability (< 10 nm) [17] and low-power consumption (1pJ/bit) [18], low operational voltage, etc.

Resistive switching has been widely investigated in various kinds of materials, such as binary oxide [19, 20], transition metal oxide[21, 22], organic materials [23, 24],

✉ S. J. Ray
ray.sjr@gmail.com; ray@iitp.ac.in

[1] Department of Physics, Indian Institute of Technology Patna, Bihta 801106, India

metal hydrogel [25], hybrid/composites, [26–28, 35] etc. In general, in oxide-based resistive switching (RS) mediums, the oxygen vacancy plays a crucial role in inducing the high/low resistance states [29–31]. Now, most oxide-based RRAM requires high-temperature processing for device fabrication. An alternative approach for the low-cost fabrication of RRAM is to use hybrid materials/composites [32, 33]. Resistive switching behavior can be easily introduced in hybrid materials/composites as we can make sufficient charge-trapping defects and interfaces [24, 34]. Various groups have fabricated RS devices by dispersed inorganic materials (metal/oxide nanoparticles) in polymer/organic matrix [26–28, 35]. From the literature survey on the resistive switching (RS) behavior observed in oxide-based composite systems, we mainly came across two types of composite systems, where RS is manifested. The first one is oxide material embedded in a polymer matrix. Here, the electro-active oxide material is added to the donor-containing polymer to induce a switching effect. Till now, most studies on such systems have been based on graphene oxide, reduced graphene oxide, ZnO, and SnO_2 nanoparticles as the electro-active oxide material [36–38]. The other type of system consists of two oxide materials, where the second oxide material assists in the increment of oxygen vacancy in the system [39, 40]. In this study, we have added LSMO as an electro-active oxide material which would provide the oxygen vacancy in the system to induce switching behavior, whereas copper iodide being a semiconductor with a bandgap of 3.1 eV, would provide an inorganic medium to transfer the electron. Now, most of the oxide-based composite systems exhibited filamentary-type resistive switching behavior, whereas, in our work, we explored the interfacial-type resistive switching considering the semiconductor behavior of copper iodide would provide low operational voltage for switching.

In our previous work, we performed [27] pulsed voltage induced resistive switching study of $(1-x)$CuI. (x)LSMO nanocomposites with $0.001 < x < 0.05$ nanocomposite system. Here, we addressed the impact of pulsewidth, delay time, duty cycle, etc., on the ON/OFF ratio. All the measurements reported in [27] have been performed using hysteretic pulse I–V measurement and square electrical pulse train I–V measurement at room temperature. Our present work investigated the DC response on $(1-x)$CuI. (x)LSMO nanocomposites by assessing the hysteretic transport measurement. We chose copper iodide, because it is a multifunctional p-type semiconductor that possesses various attractive properties like having a wide direct bandgap of 3.1 eV at room temperature, high hole mobility (> 40 cm^2 V^{-1} s^{-1} in bulk), high exciton binding energy 62 meV, electrosensitivity, and photosensitivity [43, 44]. $La_{0.7}Sr_{0.3}MnO_3$, on the other hand, was chosen as it is

a well-studied compound owing to its half-metallicity, ferromagnetism even at room temperature [45, 46].

2 Experimental details

We purchased copper iodide and the precursor chemicals (La_2O_3, $SrCO_3$, and Mn_2O_3) for the synthesis of $La_{0.7}Sr_{0.3}MnO_3$ (LSMO) from Sigma-Aldrich and all of them have a purity of at least 99.99% (see reference [47] for details of the synthesis procedure). After obtaining $La_{0.7}Sr_{0.3}MnO_3$ from the solid state synthesis route, we further ground the calcined powder for 1 h to obtain a homogeneous mixture.

To deduce the crystalline phases of CuI, $La_{0.7}Sr_{0.3}MnO_3$ and their nanocomposites, we performed X-ray diffraction (XRD) measurements. Cu-K$_\alpha$ radiation ($\lambda = 1.5406$ Å) was used in XRD with a scan rate of 2° per min and a step size of 0.02°. Transmission electron microscopy (TEM), X-ray photoelectron spectroscopy (XPS), field-emission scanning electron microscope (FESEM), and energy-dispersive X-ray spectrometry (EDS) were used to further analyse these materials. To investigate the switching behaviour of the samples, we measured transport behaviour using a two-probe approach with a Keithley 2634B source-meter on pellets with 6 mm in diameter and 2 mm in thickness. To avoid dielectric breakdown, silver contacts were employed as metal electrodes, and the compliance current was set to 100 mA. The details regarding the procedure that has been used to calculate the ON/OFF ratio have been presented in the supplementary article. The powder is taken from the area between the two electrodes of the device after terminating the SET process midway (i.e., just after altering the resistance state of the device from 'HRS' to 'LRS') the was used for Scanning Electron Microscopy (SEM), XPS, Raman Spectroscopy and Tunneling Electron Microscopy (TEM) measurement. For Raman spectroscopy, a micro-Raman spectrometer (Seki Technotron Corporation, Japan) with an integrated microscope from Olympus (×) with a He–Ne laser (wavelength, 633 nm) was used to get the Raman spectra of the nanocomposite samples.

3 Results and discussion

The XRD plots of pristine copper iodide and $La_{0.7}Sr_{0.3}MnO_3$ (LSMO) are shown in Fig.1a, b, respectively. The Rietveld refinement of copper iodide and $La_{0.7}Sr_{0.3}MnO_3$ was performed using Fullprof™ software. The statistical refinement parameters for $La_{0.7}Sr_{0.3}MnO_3$ were $R_p = 15.3$, $R_{wp} = 23.7$, $R_{exp} = 3.63$ and $\chi^2 = 3.01$. Now, the XRD plot for $x = 0.001, 0.005, 0.01, 0.02$ and 0.05 are presented in Fig.S2 in the Supporting Information section [52]. We have used Fullprof™ software to perform Rietveld refinement
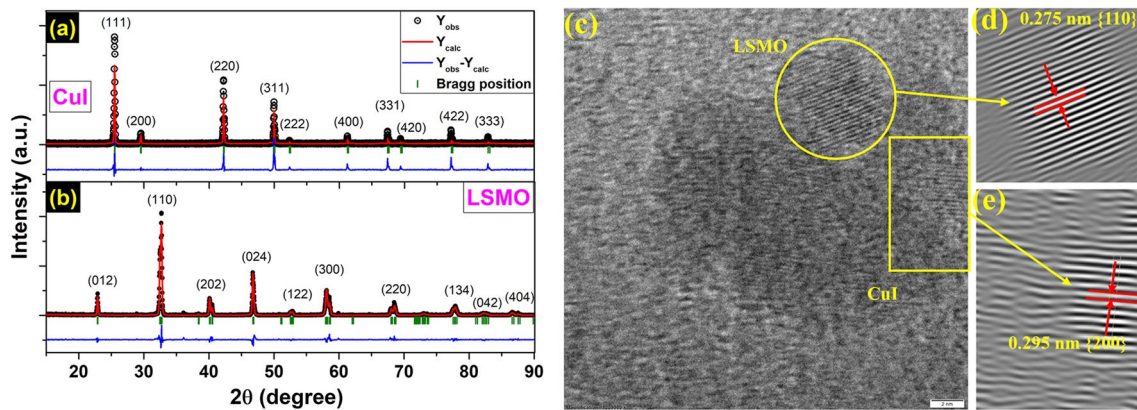
Fig. 1 Rietveld refinement pattern of the X Ray diffraction data measured for (**a**) CuI and (**b**) $La_{0.7}Sr_{0.3}MnO_3$ (LSMO). The experimentally observed, computed, and difference between curves are labelled, along with Bragg's position and Miller indices. **b** HRTEM image of nanocomposite with $x = 0.02$. **c, d** Denotes the 'd' spacing associated with LSMO and CuI, respectively

of the XRD plot of (1-x) CuI.(x) LSMO composites with R$\bar{3}$c space group for LSMO [54] and F$\bar{4}$3m for CuI [55]. The compositional analysis of the composites with varying concentrations of LSMO has been analyzed using both XRD and energy-dispersive X-ray spectroscopy (EDS). Information regarding the compositional analysis and their error limits are added in the Supporting Information section [52].

Now, to analyze the local composition of the sample, we performed HRTEM measurements. In Fig.1c, we presented the HRTEM images of the nanocomposite with $x = 0.02$. To determine the lattice parameter from the HRTEM images, we performed Fast Fourier Transform (FFT) of the selected area, as shown in Fig. 1d, e. Here, we observed two distinct inter-planar distance spacing; 0.275 nm (in Fig. 1d) and 0.295 nm (in Fig. 1e). Now, the 'd' spacing 0.295 nm associated with peak of copper iodide ($2\theta = 29.26°$) having a plane of {200}. On the other hand, the 'd' spacing 0.275 nm corresponds to the peak of $La_{0.7}Sr_{0.3}MnO_3$ $2\theta = 32.49°$ having a plane of {110}.

3.1 Resistive switching behavior in (1-x)CuI. (x) $La_{0.7}Sr_{0.3}MnO_3$ composite samples at room temperature

We performed the current–voltage measurement at room temperature by applying voltage in 0 V → 4 V → − 4 V → 0 V order, where the sweep rate was set to be 0.5 V/s. Then, we repeated the hysteretic I–V measurement for 100 consecutive cycles in a single sequence for all the nanocomposites.

Here, pristine copper iodide exhibited a minute hysteretic I–V pattern in the transport measurement which is presented in Fig.S9 in the Supporting Information section [52]. We observed a minute hysteresis in the reset process. To understand the conduction mechanism, we have plotted

log(I)–log(V). Here, we can divide the high resistance state (HRS) region (path '3') in three different sections with slopes of 1.4, 1.96, and 1.5, respectively. Therefore, as we increased the bias, the slope increased from 1.4 to ≈ 2, which follows Child's square law corresponding to the trap-controlled space-charge limited conduction (SCLC) model. Therefore, the increment in slope from 1.4 to ≈ 2 indicates the progressive filling of the generated traps and the approach of the Fermi level toward the conduction band. Upon further increasing the bias, the slope decrease to 1.5, referring to the diminished rate of trap-assisted electron transport in the system. Hysteretic I–V plot for 1st, 50th and 100th cycle for $x = 0.001$ and 0.02 are presented in Fig. 2a, b. Similar plots for $x = 0.005$ and 0.01 are shown in Fig. S11a, b in the Supporting Information section [52]. Now, in the positive polarity of Fig. 2a, the device transitioned from a high resistance state (path '1') to a low resistance state (path '2'), which is a 'Set' procedure. In negative polarity, on the other hand, the device progressed from a low resistance state (route '3') to a high resistance state (path '4'), which is the 'Reset' operation. Overall, the device demonstrated bipolar resistive switching. Additionally, we also observed that the nanocomposite did not show any drastic deviation in the I–V plots over 100 cycles of the measurement. For $x = 0.005$ and 0.01, we also observed similar resistive switching behavior. The nanocomposite with $x = 0.05$ showed linear current–voltage relation, so no hysteresis was observed in Fig.S11c, which was included in the Supporting Information section [52].

To further investigate the robustness of the resistive switching behavior, we examined the ON/OFF ratio derived from the I–V curves recorded during RS cycling through a DC voltage sweep. Figure2c, d represents the R_{OFF}, R_{ON} value and corresponding ON/OFF ratio for $x = 0.001$ for 100 cycles. In the endurance test for
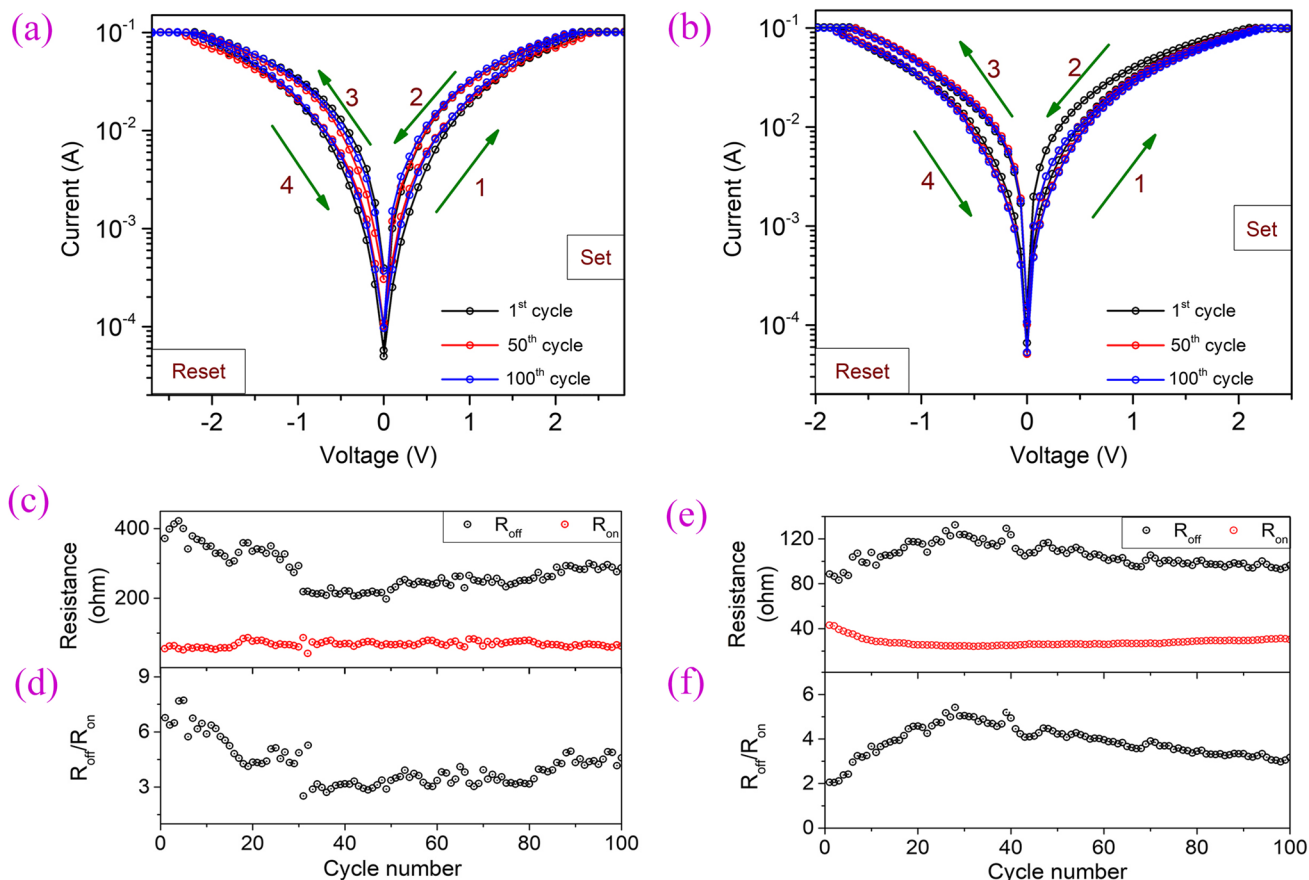
Fig. 2 a Hysteretic I–V plots of 1st, 50th and 100th cycle for (**a**) x = 0.001 and (**b**) x = 0.02. (**c**) and (**d**) represents the R_{on}, R_{off} value and corresponding ON/OFF ratio for each consecutive cycle for 100th cycles for x = 0.001 at T = 300 K. (**e**) and (**f**) Represents similar plots for x = 0.02 at T = 300 K

nanocomposite with x = 0.001, irregularity in the resistance of high resistance state at read voltage (R_{off}) up to 30 cycles that have been reflected in the fluctuations in the ON/OFF ratio. Now, we know that higher oxygen deficiency leads to a higher Schottky barrier at the interface [53]. Therefore, We are assuming that as the concentration of LSMO is quite sparse for x = 0.001 nanocomposite sample, it took around 30 cycles to set up stable pathways for migration of oxygen vacancy to/from the electrode as a function of the bias voltage. After 30 hysteresis cycles, we observed a stable switching between R_{off} and R_{on} value. Similar plots for x = 0.02 are presented in Fig. 2e, f. In addition, we also calculated the statistical distribution variables like mean and standard deviation using the following formulas:

$$mean = \mu = \tilde{x} = \frac{\sum x}{n} \tag{1}$$

and standard deviation

$$SD = \sigma = \sqrt{\frac{\sum(x - \tilde{x})^2}{n - 1}} \tag{2}$$

where 'n' indicates total switching cycles.

The average ON/OFF ratio over 100 cycles was 4.2 ± 1.1 and 3.8 ± 0.3 for x = 0.001 and 0.02, respectively.

3.2 Charge transport properties and switching mechanisms

In Fig. 3a, b, we have presented the log–log I–V plot for both the 'Set' and 'Reset' processes for x = 0.001. The high resistance state (HRS) of the 'Set' process (path '1' in Fig. 3a can be divided into two regions with (i) nonlinear behavior ($I \propto V^{1.7}$) at low bias region and (ii) child's square law, ($I \propto V^2$) at higher bias region. Now, the HRS of the 'Reset' process (path '4' in Fig. 3b) can also be segmented into two nonlinear regions, (i) $I \propto V^{1.5}$, (ii) $I \propto V^2$, i.e., child's
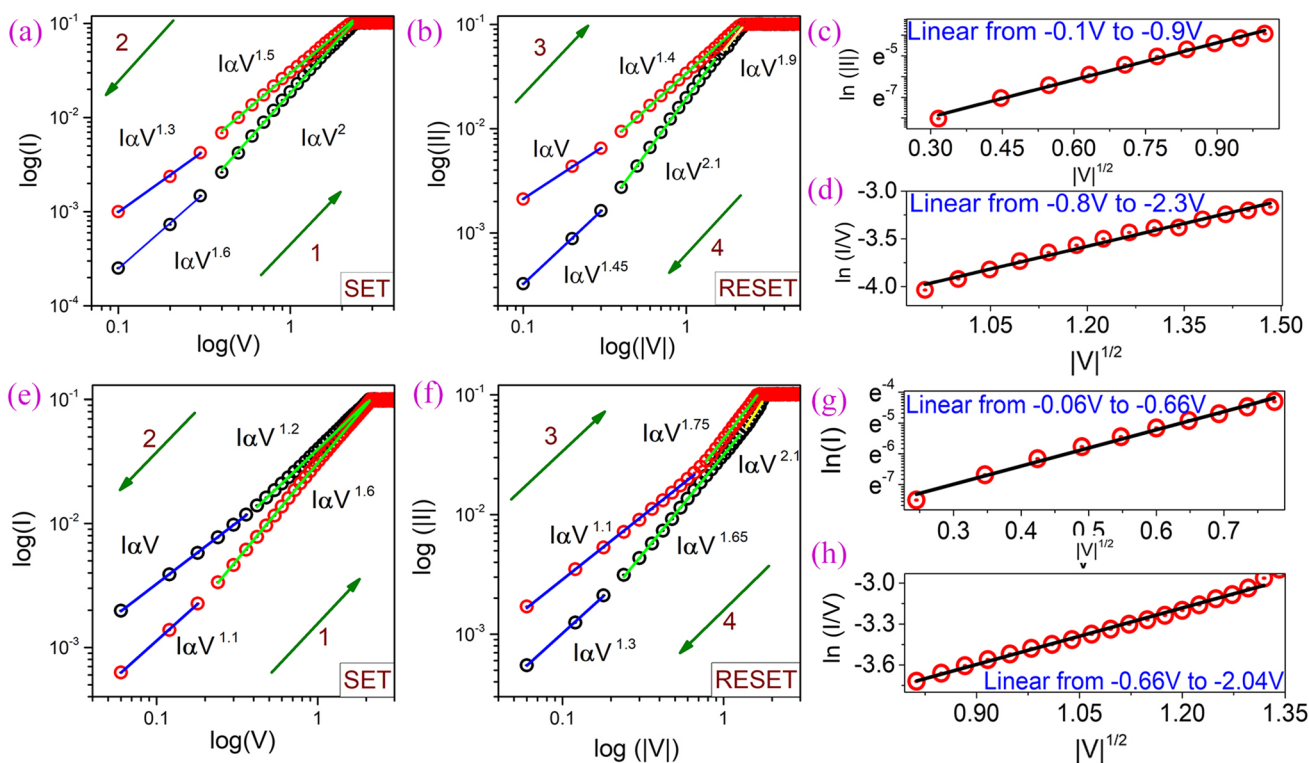
Fig. 3 a Log–log I–V plot of positive polarity ('SET' process) and **b** log–log $|I| - |V|$ plot of negative polarity ('RESET' process) for $x = 0.001$. Linear fitting of (**c**) ln(|I|)-$\sqrt{|V|}$ for Schottky Emission (SE) and (**d**) ln(|I/V|)-$\sqrt{|V|}$ for Poole–Frenkel (P–F) effect (path '4' in Fig. 2h) for $x = 0.001$. **e, f** analogous to **a–d** for $x = 0.02$

square law. On the other hand, for $x = 0.02$ (see Fig. 3e), the HRS of the 'Set' process can be divided into two regions exhibiting (i) linear behavior ($I \propto V^{1.2}$) at low voltage region, (ii) nonlinear behavior ($I \propto V^{1.6}$) at higher voltage region. Now, the HRS of the 'Reset' process (see Fig. 3f) can be categorized into three regions (i) low bias regime where $I \propto V^{1.3}$ (which can be approximated to V), i.e., Ohmic conduction mechanism, (ii) nonlinear region where $I \propto V^{1.7}$ and, (iii) increment in the current where $I \propto V^{2.1}$; these can be approximated to Child's square law ($\approx V^2$). Now, the analysis of the log–log I–V plot indicated the possibility of the existence of two separate charge transport mechanisms being dominant in different segments of the nonlinear region. Therefore, we matched the I–V plot with the current–voltage relationship associated with various conduction methods.

Next, we fitted the I–V data of the HRS region (see path '4' of Fig. 3b) of the negative polarity with (a) ln(|I|) vs. $\sqrt{|V|}$ and (b) ln|(I/V)| vs. $\sqrt{|V|}$. From the linear fitting, we got (i) Schottky emission (SE) to be dominant in -0.1 V to -0.9 V region (confirmed by the linear fitting of ln(I) vs. $\sqrt{|V|}$ plot in Fig. 3c) and (ii) Poole–Frenkel (P–F) effect was dominant in -0.8 V to -2.3 V for $x = 0.001$ (see Fig. 3d). On the other hand, for $x = 0.02$: (i) Schottky emission (SE) was dominant from -0.06 V to -0.66 V and (ii) Poole–Frenkel (P–F) effect was dominant from -0.66 V to

-2.04 V supported by the linear fitting of the corresponding region (see Fig. 3g, h). Thus, our findings agree well with our previous work [27] where Schottky emission (which follows ln(|I|) vs. $\sqrt{|V|}$ relation) and Poole–Frenkel effect (which follows ln|(I/V)| vs. $\sqrt{|V|}$ relation) turned out to be the main driving charge transport mechanisms in lower and higher bias regions, respectively.

Schottky emission is an interface-limited conduction mechanism that takes place when due to the application of an electric field, thermionic emission of electrons occurs over a reduced work-function barrier. Now, in the oxide-based resistive switching medium, voltage direction-dependent migration of oxygen via oxygen vacancies induces an oxygen-deficient/oxygen-rich region at the interface of electrode and resistive switching medium. This results in altering the resistance state of the switching medium. Poole–Frenkel emission, on the other hand, is a type of bulk restricted conduction that happens in the presence of a given moderate electric field as a result of field-assisted thermal excitation of trapped electrons into the conduction band, where the trapping centers are provided by defects. As the conduction mechanism of the Poole–Frenkel effect is related to trapping sites in the dielectric material, we are deducing that copper iodide acted as a dielectric medium, while LSMO provided oxygen vacancies by acting as defect traps. The

results obtained from X-ray photoelectron Spectroscopy (XPS) measurements analysis also supported this theory.

We used XPS to clarify the role of oxygen vacancies in resistive switching. In Fig. 4a, we presented the high-resolution XPS spectra for pristine CuI, nanocomposite with $x = 0.001$ and 0.02 consisting of O-1s, I-3d and, Cu-2p peaks. Here, the C-1s peak (284.6 eV) was used to calibrate the XPS curves. Now, the short-range scan of the O-1S peak was shown for CuI, $x = 0.001$ and 0.02 in Fig. S9 (in the Supporting Information section [52]), Fig. 4b–d, respectively. As we calculated the area under the peaks for CuI, $x = 0.001$ and 0.02, we observed that the area under O-1s peak for $x = 0.001$ and $x = 0.02$ were significantly higher compared to pristine copper iodide. After fitting the raw data with the multi-peaks model following Shirley's background, we were able to deconvolute the O-1S broad peak into three peaks corresponding to the binding energies 529.4 eV, 530.2 eV, and 531.4 eV, respectively. In addition, for $x = 0.02$, the triplet peaks are associated with 529.0 eV, 530.2 eV and, 531.4 eV, respectively. In general, O-1s spectra of LSMO exhibits asymmetric broadband with two or three peaks. The peak in the 528–530 eV region corresponds to the Mn-related lattice oxygen (O^{2-}). Whereas in 530–534 eV region the peaks manifest from the under-coordinated oxygen at the interface oxygen bonding with La/Sr at A sites in ABO_3 perovskite structure and/or oxygen vacancies, i.e., to the oxygen-related defects [48–50]. In addition, we also observed in the O-1S peak for x = 0.02 has (i) a sharper intensity peak at 530.2 eV compared to $x = 0.001$, which is typically associated with the oxygen vacancy, (ii) a larger area under the curve

compared to $x = 0.001$ and (iii) shifted the position of the peak corresponding to Mn–O.

In Fig. 4d, e, the peak shift of Cu-2p and I-3d towards higher binding energy as the concentration of LSMO increases is shown. Now, we know that if we modify a specimen by adding electro-negative (compared to the base element) elements or impurities, electron density around the base element will decrease, increasing the binding energy. Therefore, we will observe a shift in the positive direction in binding energy [51]. As the LSMO concentration is increased in our study, a positive shift in peak position in Cu-2p was observed. In addition, we have also calculated the ratio of area under the Cu-$2p_{3/2}$ and Cu-$2p_{1/2}$ peaks for CuI, $x = 0.001$ and 0.02 which can be found in Table S1 in the Supporting Information section [52]. The ratio of area under the Cu-$2p_{3/2}$ and Cu-$2p_{1/2}$ peaks for pristine copper iodide was 2.00, as predicted from a sample with no impurities. As we increased the concentration of LSMO in copper iodide the ratio between areas decreased gradually. This consolidates our previous claim regarding the role of LSMO (oxygen present in LSMO to be precise) being responsible for the chemical shift in Cu-2p peaks. Overall, we are deducing the origin of resistive switching to be the elevated presence of oxygen in the sample, which occurred because of oxygen migration from the area adjacent to the metal electrode. The migration of oxygen reduced oxygen concentration (i.e., rise in the presence of oxygen vacancy) at the interface of nanocomposite and electrode. As we discussed earlier, the presence of oxygen vacancy lowers the barrier height of the Schottky barrier, which in turn helped to
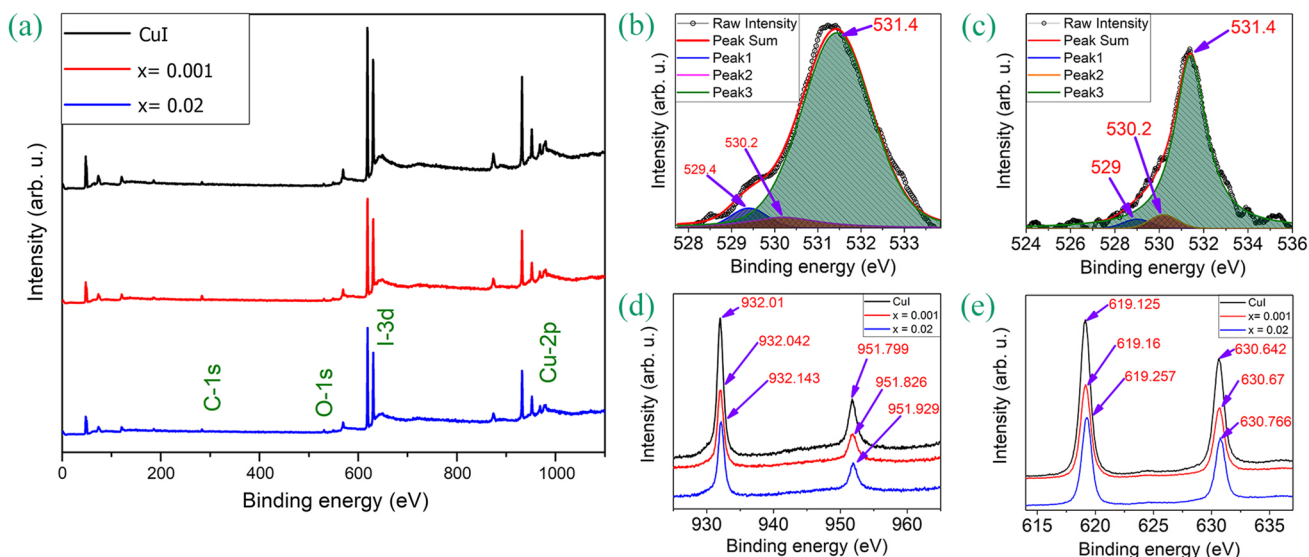

Fig. 4 **a** Wide scan range XPS spectra of pristine copper iodide, nanocomposite with **b** $x = 0.001$ and **c** $x = 0.02$. Short scan range of oxygen (O) along with fitted XPS curve of the for (**b**) $x = 0.001$ and **c** $x = 0.02$. Chemical shift of (**d**) Cu-$2p_{3/2}$ and Cu-$2p_{1/2}$ as well as (**e**) I-$3d_{5/2}$ and (**e**) I-$3d_{3/2}$ with varying concentration of LSMO in the nanocomposites

induce LRS. Therefore, essentially, the system went from 'HRS' to 'LRS'.

Now, for XPS, TEM, and SEM (see Figs. S3–S7 in the supplementary document [52]), we have used the sample taken from the intermediate area of the pellet after the 'SET' process. We did not observe the trace of silver in XPS spectra, HRTEM image or in SEM–EDX plots. Therefore, this essentially omits the possibility of the migration of silver ion as a potential reason for the emergence of resistive switching in the system.

3.3 Temperature dependence of the resistive switching behavior

To understand the impact of temperature on the conduction mechanisms and ON/OFF ratio of the nanocomposites, we have repeated the hysteretic I–V measurement at different temperatures. The hysteretic I–V plots corresponding to the nanocomposites with $x = 0.001$ and 0.02 at $T = 150$ K, 200 K, 250 K, and 300 K are presented in Fig. 5a, b respectively. The area between the hysteretic I–V plots also increased as we lowered the temperature. To analyze the conduction mechanism, we have plotted log–log I–V of the 'Reset' process for both $x = 0.001$ (see Fig. 5b) and $x = 0.02$ (see Fig. 5f). Now, the HRS of the 'Reset' process can be divided into three different regions (i) nonlinear behavior ($I \propto V^{1.4}$ for $x = 0.001$ and $I \propto V^{1.5}$ $x = 0.02$) at lower voltage region (ii) steep increase in the slope ($I \propto V^{2.4}$

for $x = 0.001$ and $I \propto V^{2.7}$ $x = 0.02$) and finally (iii) child's square law ($I \propto V^{2}$) for both $x = 0.001$ and $x = 0.02$. From the fitting of the $\ln(|I|)$ vs $\sqrt{|V|}$ and $\ln(I/V)$ vs. $\sqrt{|V|}$ curve, we got (i) Schottky emission was dominant in -0.08 V to -0.88 V region for $x = 0.001$ (see Fig. 5c) and from -0.08 V to -0.80V for $x = 0.02$ (see Fig. 5g); for higher bias region (ii) Poole–Frenkel effect was dominant from -0.96 V to -1.68 V (see Fig. 5d) for $x = 0.001$ and from -0.80 V to -1.52 V for $x = 0.02$ (see Fig. 5h). We did similar analysis for $x = 0.001$ and $x = 0.02$ at $T = 200$ K and 150 K. In all the cases, the HRS of the 'Reset' process was dictated by Schottky emission at lower bias region and Poole–Frenkel emission at higher bias region.

For the endurance test of $x = 0.001$, 0.02 at $T = 250$ K, the 'Set'–'Reset' process was repeated for 100 consecutive cycles in a single sequence. The hysteretic I–V plot for 1st, 50th and 100th cycles for both samples are shown in Fig. S12 in the Supporting Information section [52]. Here, we observed that the deviation of the path of the I–V pattern of 1st from 50th and 50th from 100th cycle differs slightly (both for $x = 0.001$ and $x = 0.02$). R_{off}, R_{on} value and their ratio at $T = 250$ K are presented in Fig. 6a, b for $x = 0.001$ and Fig. 6c, d for $x = 0.02$, respectively. The average ON/OFF ratio was 19.8 ± 1.8 for $x = 0.001$ and 22.7 ± 4.1 for $x = 0.02$. Now, at $T = 200$ K and 150 K for $x = 0.001$ average ON/OFF ratio was 9.6 ± 1.8 and 2.9 ± 0.2; and for $x = 0.02$ average ON/OFF ratio was 12.7 ± 0.8 and
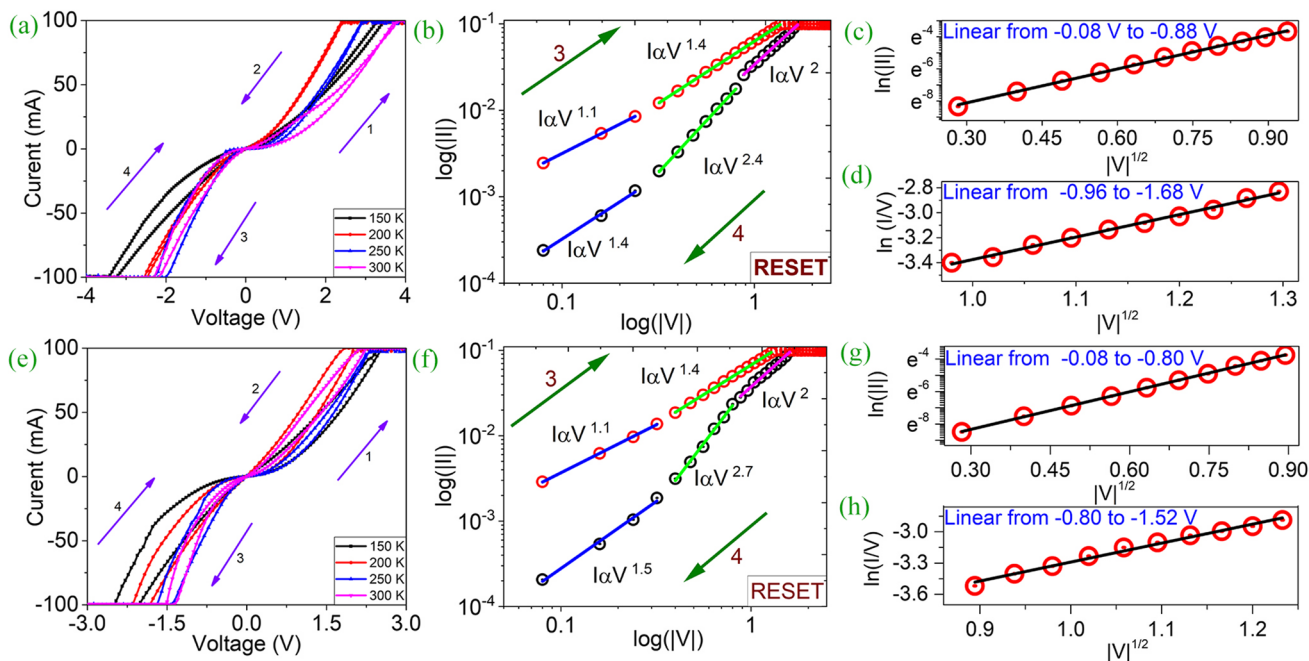
Fig. 5 **a** Hysteretic I–V curve for $x = 0.001$ temperature $T = 150$ K, 200 K, 250 K, 300 K. **b** log–log I–V of negative polarity for $x = 0.001$ at $T = 250$K. **c** $\ln(|I|)$-$\sqrt{|V|}$ for SE (or negative polarity) and **(d)** $\ln(|I/V|)$-$\sqrt{|V|}$ for P–F. (or negative polarity) for $x = 0.001$ at $T = 250$K. **e–h** are analogous to **a–d** for $x = 0.02$
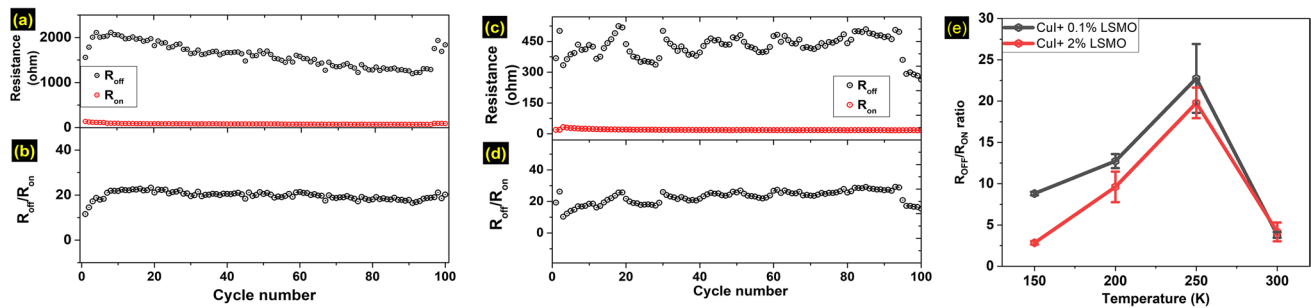
Fig. 6 R_{on}, R_{off} value for each consecutive cycle for upto 100th cycle for (**a**) $x = 0.001$ and (**c**) $x = 0.02$ at $T = 250$ K. Variation of averaged ON/OFF ratio over 100 cycles at $x = 0.001$ and 0.02 for 150 K to 300 K

8.8 ± 0.2, respectively (see Fig. S12 in the supplementary document [52]). We did not observe any specific pattern of rising/diminishing value of ON/OFF ratio as we varied the concentration of LSMO in the nanocomposite. The reason behind the fall in ON/OFF ratio at a temperature lower than 250 K might be associated with the localization of the oxygen ions. As the localized ions lack sufficient thermal energy to cross the barrier or hop from one trapping site to the other. Therefore, the oxygen vacancy sites get partially filled because of reduced migration of oxygen ions which can lead to the reduction in current.

In our work, we explored the idea of enhancing the performance of RS medium (pristine copper iodide) with the addition of impurity (LSMO). Although at room temperature, the impact of LSMO on the resistive switching properties was not apparent, as we lowered the temperature, it became prominent. We observed the optimal temperature for the operation of resistive switching is 250 K. The underlying reason behind this drastic change can be associated with the contribution of oxygen vacancy in the system because of LSMO. As it is portrayed in the short scan of O-1S peak of $x = 0.001$ and $x = 0.02$ (see Fig. 3a, b), in both samples, the peak corresponding to oxygen vacancy was present. As we have seen from the cases with a high ON/OFF ratio, HRS showed nonlinear behavior even at low bias voltage, and LRS showed ohmic behavior. We conclude that the nonlinearity at low voltage is directly associated with the oxygen vacancy peak owing to LSMO. Another trend we observed was that as the LSMO concentration increased in copper iodide, the overall performance in terms of the ON/OFF ratio also improved at lower temperature regions (see Fig. 5b and d). At 250 K and 200 K, both $x = 0.001$ and $x = 0.02$ exhibited comparable ON/OFF ratio whereas we further lowered the temperature (150K) $x = 0.02$ exhibited higher ON/OFF ratio. Another thing we observed is that $x = 0.02$ demonstrated a more stable result (denoted by the smaller value of the standard deviation in the ON/OFF ratio) at $T = 300$ K, 200 K, and 150 K. On the other hand, at $T = 250$ K, $x = 0.001$ demonstrated a more stable ON/OFF ratio variation.

4 Conclusion

To summarize, temperature-dependent resistive switching behavior was studied for (1-x)CuI.(x)LSMO nanocomposites with $0.001 < x < 0.05$. Resistive switching responses were stable over 100 repeated cycles of hysteretic I–V measurement for all the samples. The highest ON/OFF ratio averaged over 100 cycles for $x = 0.001$ and 0.02 were 19.8 ± 1.8 and 22.7 ± 4.1, respectively (at 250 K). From the analysis of the I–V plots, it turned out that Schottky emission and Poole–Frenkel were the dominant conduction mechanism for the low bias and high bias segment of the nonlinear region, respectively. The enhanced switching response of the RS medium after the addition of LSMO can be associated with the oxygen vacancy-induced conduction which was confirmed by XPS. The results above provide insight into how we can alter the resistive switching behavior by adding impurity to the specimen and also how temperature affects the ON/OFF ratio in an RS medium.

References

1. R. Waser, R. Dittmann, S. Menzel, T. Noll, Introduction to new memory paradigms: memristive phenomena and neuromorphic applications. Faraday Discuss. **213**, 11 (2019). https://doi.org/10.1039/c8fd90058b

2. D.S. Jeong, C.S. Hwang, Nonvolatile memory materials for neuromorphic intelligent machines. Adv. Mater. **30**, 1704729 (2018). https://doi.org/10.1002/adma.201704729

3. R. Bez, A. Pirovano, Overview of non-volatile memory technology: markets, technologies and trends, in booktitle Advances in

Non-volatile Memory and Storage Technology (publisher Elsevier, 2014) pp. 1–24 https://doi.org/10.1533/9780857098092.1

4. G.W. Burr, R.M. Shelby, A. Sebastian, S. Kim, S. Kim, S. Sidler, K. Virwani, M. Ishii, P. Narayanan, A. Fumarola, L.L. Sanches, I. Boybat, M.L. Gallo, K. Moon, J. Woo, H. Hwang, Y. Leblebici, Neuromorphic computing using non-volatile memory. Adv. Phys. X **2**, 89 (2016). https://doi.org/10.1080/23746149.2016.1259585

5. L. Peng, Z. Li, G. Wang, J. Zhou, R. Mazzarello, Z. Sun, Reduction in thermal conductivity of sb2te phase-change material by scandium/yttrium doping. J. Alloy. Compd. **821**, 153499 (2020). https://doi.org/10.1016/j.jallcom.2019.153499

6. Q. Wang, G. Niu, R. Wang, R. Luo, Z.-G. Ye, J. Bi, X. Li, Z. Song, W. Ren, S. Song, Reliable ge2sb2te5 based phase-change electronic synapses using carbon doping and programmed pulses. J. Materiomics (2021). https://doi.org/10.1016/j.jmat.2021.08.004

7. A.D. Kent, D.C. Worledge, A new spin on magnetic memories. Nat. Nanotechnol. **10**, 187 (2015). https://doi.org/10.1038/nnano.2015.24

8. T. Kawahara, K. Ito, R. Takemura, H. Ohno, Spin-transfer torque RAM technology: review and prospect. Microelectron. Reliab. **52**, 613 (2012). https://doi.org/10.1016/j.microrel.2011.09.028

9. H. Shen, J. Liu, K. Chang, L. Fu, In-plane ferroelectric tunnel junction. Phys. Rev. Appl. **11**, 024048 (2019). https://doi.org/10.1103/physrevapplied.11.024048

10. K. Kumari, A. Kumar, A.D. Thakur, S. Ray, Charge transport and resistive switching in a 2d hybrid interface. Mater. Res. Bull. **139**, 111195 (2021). https://doi.org/10.1016/j.materresbull.2020.111195

11. P.M. Chowdhury, A. Raychaudhuri, Electromigration of oxygen and resistive state transitions in sub-micron width long strip of la0.85sr0.15mno3 connected to an engineered oxygen source. Mater. Res. Bull. **137**, 111160 (2021). https://doi.org/10.1016/j.materresbull.2020.111160

12. J. Jia, J. Gao, Y. He, G. Zhao, Y. Ren, Resistive switching effect of YBa2cu3o7–x/nb:SrTiO3 heterostructure. Mater. Res. Bull. **107**, 328 (2018). https://doi.org/10.1016/j.materresbull.2018.08.005

13. C.-A. Lin, C.-J. Huang, T.-Y. Tseng, Impact of barrier layer on HfO2-based conductive bridge random access memory. Appl. Phys. Lett. **114**, 093105 (2019). https://doi.org/10.1063/1.5087421

14. K. Hong, K.K. Min, M.-H. Kim, S. Bang, T.-H. Kim, D.K. Lee, Y.J. Choi, C.S. Kim, J.Y. Lee, S. Kim, S. Cho, B.-G. Park, Investigation of the thermal recovery from reset breakdown of a SiN x -based RRAM. IEEE Trans. Electron Devices **67**, 1600 (2020). https://doi.org/10.1109/ted.2020.2976106

15. K.-M. Persson, M.S. Ram, O.-P. Kilpi, M. Borg, L.-E. Wernersson, Cross-point arrays with low-power ITO-HfO 2 resistive memory cells integrated on vertical III–v nanowires. Adv. Electron. Mater. **6**, 2000154 (2020). https://doi.org/10.1002/aelm.202000154

16. B. Sánta, D. Molnár, P. Haiber, A. Gubicza, E. Szilágyi, Z. Zolnai, A. Halbritter, M. Csontos, Nanosecond resistive switching in ag/AgI/PtIr nanojunctions. Beilstein J. Nanotechnol. **11**, 92 (2020). https://doi.org/10.3762/bjnano.11.9

17. G. Zisis, C.Y.J. Ying, P. Ganguly, C.L. Sones, E. Soergel, R.W. Eason, S. Mailis, Enhanced electro-optic response in domain-engineered LiNbO3 channel waveguides. Appl. Phys. Lett. **109**, 021101 (2016). https://doi.org/10.1063/1.4958685

18. X. Ding, Y. Feng, P. Huang, L. Liu, J. Kang, Low-power resistive switching characteristic in HfO2/TiOx bi-layer resistive random-access memory. Nanoscale Res. Lett. (2019). https://doi.org/10.1186/s11671-019-2956-4

19. D.-H. Kwon, S. Lee, C.S. Kang, Y.S. Choi, S.J. Kang, H.L. Cho, W. Sohn, J. Jo, S.-Y. Lee, K.H. Oh, T.W. Noh, R.A.D. Souza, M. Martin, M. Kim, Unraveling the origin and mechanism of nano-filament formation in polycrystalline SrTiO 3 resistive switching

20. Y.B. Lin, Z.B. Yan, X.B. Lu, Z.X. Lu, M. Zeng, Y. Chen, X.S. Gao, J.G. Wan, J.Y. Dai, J.-M. Liu, Temperature-dependent and polarization-tuned resistive switching in au/BiFeO3/SrRuO3 junctions. Appl. Phys. Lett. **104**, 143503 (2014). https://doi.org/10.1063/1.4870813

21. C. Mahata, C. Lee, Y. An, M.-H. Kim, S. Bang, C.S. Kim, J.-H. Ryu, S. Kim, H. Kim, B.-G. Park, Resistive switching and synaptic behaviors of an HfO2/al2o3 stack on ITO for neuromorphic systems. J. Alloy. Compd. **826**, 154434 (2020). https://doi.org/10.1016/j.jallcom.2020.154434

22. H. Zhang, S. Yoo, S. Menzel, C. Funck, F. Cüppers, D.J. Wouters, C.S. Hwang, R. Waser, S. Hoffmann-Eifert, Understanding the coexistence of two bipolar resistive switching modes with opposite polarity in pt/TiO2/ti/pt nanosized ReRAM devices. ACS Appl. Mater. Interfaces **10**, 29766 (2018). https://doi.org/10.1021/acsami.8b09068

23. N. Raeis-Hosseini, J.-S. Lee, Resistive switching memory using biomaterials. J. Electroceramics **39**, 223 (2017). https://doi.org/10.1007/s10832-017-0104-z

24. S. Gao, X. Yi, J. Shang, G. Liu, R.-W. Li, Organic and hybrid resistive switching materials and devices. Chem. Soc. Rev. **48**, 1531 (2019). https://doi.org/10.1039/c8cs00614h

25. A. Noohul, S. Majumder, S. Jyoti Ray, A wide bandgap semiconducting magnesium hydrogel: moisture harvest, iodine sequestration, and resistive switching. Langmuir **38**(34), 10601–10610 (2022)

26. D. Chaudhary, S. Munjal, N. Khare, V.D. Vankar, Bipolar resistive switching and nonvolatile memory effect in poly (3-hexylthiophene) -carbon nanotube composite films. Carbon **130**, 553 (2018). https://doi.org/10.1016/j.carbon.2018.01.058

27. S. Majumder, K. Kumari, S.J. Ray, Pulsed voltage induced resistive switching behavior of copper iodide and la0.7sr0.3mno3 nanocomposites. Mater. Lett. **302**, 130339 (2021). https://doi.org/10.1016/j.matlet.2021.130339

28. E. Ercan, J.-Y. Chen, P.-C. Tsai, J.-Y. Lam, S.C.-W. Huang, C.-C. Chueh, W.-C. Chen, A redox-based resistive switching memory device consisting of organic-inorganic hybrid perovskite/polymer composite thin film. Adv. Electron. Mater. **3**, 1700344 (2017). https://doi.org/10.1002/aelm.201700344

29. K. Karuna, S.J. Ray, A.D. Thakur, Resistive switching phenomena: a probe for the tracing of secondary phase in manganite. Appl. Phys. A **128**(5), 1–11 (2022)

30. K. Karuna, A.D. Thakur, S.J. Ray, Structural, resistive switching and charge transport behaviour of (1-x) La 0.7 Sr 0.3 MnO 3.(x) ZnO composite system. Appl. Phys. A **128**(11), 992 (2022)

31. K. Karuna, A.D. Thakur, S.J. Ray, The effect of graphene and reduced graphene oxide on the resistive switching behavior of La0. 7Ba0. 3MnO3. Mater. Today Commun. **26**, 102040 (2021)

32. K. Karuna, S. Kar, A.D. Thakur, S.J. Ray, Role of an oxide interface in a resistive switch. Curr. Appl. Phys. **35**, 16–23 (2022)

33. K. Karuna, S. Majumder, A.D. Thakur, S.J. Ray, Temperature-dependent resistive switching behaviour of an oxide memristor. Mater. Lett. **303**, 130451 (2021)

34. K. Ashutosh, K. Kumari, S.J. Ray, A.D. Thakur, Graphene mediated resistive switching and thermoelectric behavior in lanthanum cobaltate. J. Appl. Phys. **127**(23), 235103 (2020)

35. V.K. Perla, S.K. Ghosh, K. Mallick, Light induced transformation of resistive switching polarity in sb2s3 based organic-inorganic hybrid devices. J. Mater. Chem. C (2021). https://doi.org/10.1039/d1tc01121a

36. W. Yu, F. Chen, Y. Wang, L. Zhao, Rapid evaluation of oxygen vacancies-enhanced photogeneration of the superoxide radical in nano-TiO$_2$ suspensions. RSC Adv. **10**, 29082 (2020). https://doi.org/10.1039/d0ra06299e

37. D. Chen, Y. Wang, Z. Lin, J. Huang, X. Chen, D. Pan, F. Huang, Growth strategy and physical properties of the high mobility p-type CuI crystal. Crystal Growth Design **10**, 2057 (2010). https://doi.org/10.1021/cg100270d

38. J. Dhanalakshmi, S. Iyyapushpam, S.T. Nishanthi, M. Malligavathy, D.P. Padiyan, Investigation of oxygen vacancies in ce coupled TiO_2 nanocomposites by Raman and PL spectra. Adv. Nat. Sci. Nanosci. Nanotechnol. **8**, 015015 (2017). https://doi.org/10.1088/2043-6254/aa5984

39. S. Choudhary, M. Soni, S.K. Sharma, Low voltage controlled switching of MoStextsubscript2 -GO resistive layers based ReRAM for non-volatile memory applications. Semicond. Sci. Technol. **34**, 085009 (2019). https://doi.org/10.1088/1361-6641/ab2c09

40. G. Khurana, P. Misra, N. Kumar, R.S. Katiyar, Tunable power switching in nonvolatile flexible memory devices based on graphene oxide embedded with ZnO nanorods. J. Phys. Chem. C **118**, 21357 (2014). https://doi.org/10.1021/jp506856f

41. L. Cao, O. Petracic, P. Zakalek, A. Weber, U. Rücker, J. Schubert, A. Koutsioubas, S. Mattauch, T. Brückel, Reversible control of physical properties via an oxygen-vacancy-driven topotactic transition in epitaxial la0.7 sr0.3 MnO3-δ thin films. Adv. Mater. **31**, 1806183 (2018). https://doi.org/10.1002/adma.201806183

42. L. Yao, S. Inkinen, S. van Dijken, Direct observation of oxygen vacancy-driven structural and resistive phase transitions in la2/3sr1/3mno3. Nat. Commun. (2017). https://doi.org/10.1038/ncomms14544

43. P. Sirimanne, M. Rusop, T. Shirata, T. Soga, T. Jimbo, Characterization of transparent conducting CuI thin films prepared by pulse laser deposition technique. Chem. Phys. Lett. **366**, 485 (2002). https://doi.org/10.1016/s0009-2614(02)01590-7

44. N.P. Klochko, K.S. Klepikova, V.R. Kopach, D.O. Zhadan, V.V. Starikov, D.S. Sofronov, I.V. Khrypunova, S.I. Petrushenko, S.V. Dukarov, V.M. Lyubov, M.V. Kirichenko, S.P. Bigas, A.L. Khrypunova, Solution-produced copper iodide thin films for photosensor and for vertical thermoelectric nanogenerator, which uses a spontaneous temperature gradient. J. Mater. Sci.: Mater. Electron. **30**, 17514 (2019). https://doi.org/10.1007/s10854-019-02103-4

45. J.-H. Park, E. Vescovo, H.-J. Kim, C. Kwon, R. Ramesh, T. Venkatesan, Magnetic properties at surface boundary of a half-metallic FerromagnetLa0.7sr0.3mno3. Phys. Rev. Lett. **81**, 1953 (1998). https://doi.org/10.1103/physrevlett.81.1953

46. N. Kallel, S. Kallel, A. Hagaza, M. Oumezzine, Magnetocaloric properties in the cr-doped la0.7sr0.3mno3 manganites. Physica B **404**, 285 (2009). https://doi.org/10.1016/j.physb.2008.10.049

47. K. Kumari, A. Kumar, D.K. Kotnees, J. Balakrishnan, A.D. Thakur, S. Ray, Structural and resistive switching behaviour in lanthanum strontium manganite—reduced graphene oxide nanocomposite system. J. Alloy. Compd. **815**, 152213 (2020). https://doi.org/10.1016/j.jallcom.2019.152213

48. X. Zhang, X. Kan, M. Wang, R. Rao, N. Qian, G. Zheng, Y. Ma, Mechanism of enhanced magnetization in CoFe2o4/la0.7sr0.3mno3 composites with different mass ratios. Ceram. Int. **46**, 14847 (2020). https://doi.org/10.1016/j.ceramint.2020.03.010

49. E. Beyreuther, S. Grafström, L.M. Eng, C. Thiele, K. Dörr, XPS investigation of mn valence in lanthanum manganite thin films under variation of oxygen content. Phys. Rev. B **73**, 155425 (2006). https://doi.org/10.1103/physrevb.73.155425

50. R. Das, T. Sarkar, K. Mandal, Multiferroic properties of ba2+and gd3+co-doped bismuth ferrite: magnetic, ferroelectric and impedance spectroscopic analysis. J. Phys. D Appl. Phys. **45**, 455002 (2012). https://doi.org/10.1088/0022-3727/45/45/455002

51. M.T. Greiner, L. Chai, M.G. Helander, W.-M. Tang, Z.-H. Lu, Transition metal oxide work functions: the influence of cation oxidation state and oxygen vacancies. Adv. Funct. Mater. **22**, 4557 (2012). https://doi.org/10.1002/adfm.201200615

52. S. Majumder, et al., for Additional Results on Temperature-dependent resistive switching behavior of a hybrid semiconductor-oxide planar system. https://doi.org/10.1007/s00339-023-06616-y

53. K. Komal, G. Gupta, M. Singh, B. Singh, Improved resistive switching of RGO and SnO2 based resistive memory device for non-volatile memory application. J. Alloy. Compd. **923**, 166196 (2022). https://doi.org/10.1016/j.jallcom.2022.166196

54. S.J. Hibble, S.P. Cooper, A.C. Hannon, I.D. Fawcett, M. Greenblatt, Local distortions in the colossal magnetoresistive manganates la0.70ca0.30mno3, la0.80ca0.20mno3and la0.70sr0.30mno3revealed by total neutron diffraction. J. Phys.: Condens. Matter **11**, 9221 (1999). https://doi.org/10.1088/0953-8984/11/47/308

55. R.W.G. Wyckoff, E. Posnjak, The crystal structures of the cuprous halides. J. Am. Chem. Soc. (1922). https://doi.org/10.1021/ja01422a005